atmosphere

MDPI

Article

# Profiling Radar Observations and Numerical Simulations of a Downslope Wind Storm and Rotor on the Lee of the Medicine Bow Mountains in Wyoming

**Binod Pokharel, Bart Geerts *, Xia Chu and Philip Bergmaier**

Department of Atmospheric Science, University of Wyoming, Laramie, WY 82071, USA; binod52@gmail.com (B.P.); xchu1@uwyo.edu (X.C.); pbergmai@uwyo.edu (P.B.)

* Correspondence: geerts@uwyo.edu; Tel.: +1-307-766-2261

Academic Editor: Vanda Grubišić

Received: 24 October 2016; Accepted: 13 February 2017; Published: 15 February 2017

**Abstract:** This study describes a downslope wind storm event observed over the Medicine Bow range (Wyoming, USA) on 11 January 2013. The University of Wyoming King Air (UWKA) made four along-wind passes over a five-hour period over the mountain of interest. These passes were recognized as among the most turbulent ones encountered in many years by crew members. The MacCready turbulence meter aboard the UWKA measured moderate to severe turbulence conditions on each pass in the lee of the mountain range, with eddy dissipation rate values over 0.5 $m^{2/3}$ $s^{-1}$. Three rawinsondes were released from an upstream location at different times. This event is simulated using the non-hydrostatic Weather Research and Forecast (WRF) model at an inner-domain resolution of 1 km. The model produces a downslope wind storm, notwithstanding some discrepancies between model and rawinsonde data in terms of upstream atmospheric conditions. Airborne Wyoming Cloud Radar (WCR) vertical-plane Doppler velocity data from two beams, one pointing to the nadir and one pointing slant forward, are synthesized to obtain a two-dimensional velocity field in the vertical plane below flight level. This synthesis reveals the fine-scale details of an orographic wave breaking event, including strong, persistent downslope acceleration, a strong leeside updraft (up to 10 $m \cdot s^{-1}$) flanked by counter-rotating vortices, and deep turbulence, extending well above flight level. The analysis of WCR-derived cross-mountain flow in 19 winter storms over the same mountain reveals that cross-mountain flow acceleration and downslope wind formation are difficult to predict from upstream wind and stability profiles.

**Keywords:** downslope wind storm; hydraulic jump; rotor; turbulence; Wyoming Cloud Radar

## 1. Introduction

Downslope wind storms sometimes occur on the lee of mountain ranges such as the Rocky Mountain Front Range (e.g., [1–4]). Such terrain-induced non-linear flow phenomena can result in damaging surface winds as well as severe turbulence both near the ground and at higher levels, thus affecting flight safety (e.g., [5,6]). The strong near-surface downslope winds may halt in a narrow convergence zone, resulting in a deep, turbulent updraft. Several aircraft accidents have been attributed to turbulence associated with downslope wind storms [3,7]. A rich array of instruments was deployed in the 2006 Terrain-induced Rotor Experiment (T-REX) to study downslope wind storms and related phenomena in the Owens Valley, California, in the lee of the Sierra Nevada [8].

Several theories have been proposed for the downslope acceleration of flow and the sudden, steep ascent further downwind [9,10]. The main theories assume either an internal hydraulic jump [5,11,12], or gravity wave energy reflection on a self-induced critical level and local resonance (resonant

amplification theory) [13–15]. Both theories require strong low-level flow across the mountain range, and a weakly stratified layer overlying a stable layer that immerses the terrain. The stable layer is squeezed over the terrain crest and then plunges into the lee, much like supercritical water flows over a barrier before encountering a hydraulic jump to transition back to subcritical flow. The high-amplitude hydraulic jump or wave energy reflection typically results in wave breaking and turbulence over a depth that usually exceeds the height of the terrain crest, and even the height of the equilibrium level of the potentially warm air carried down in the lee.

The tremendous shear along the upper edge of this plunging flow, as well as near the surface, can produce severe turbulence. The breaking of waves aloft near the top of the hydraulic jump, and occasionally the release of static instability due to overturning isentropic streamlines [16], may also cause severe turbulence. The hydraulic jump is associated with intense low-level convergence. The opposing low-level flow (encountered sometimes further downwind of the mountain) is part of a horizontal vortex referred to as a rotor, which poses an additional threat to aircraft during landing or take-off. Rotors form due to boundary layer separation that may develop in association with the leading updraft in hydraulic jumps, but may also be associated with high-amplitude trapped lee waves [17]. A counter-rotating vortex (or local horizontal vorticity maximum) is also found on the opposite side of the hydraulic jump; it is a reflection of the negative shear at the upper margin of the plunging current [17]. The strength and depth of the upstream stable layer strongly affect the amplitude of the downslope wind storm and the intensity of lee rotors [12,18–20].

The present study documents a downslope wind storm, a deep updraft and rotors in the lee of the Medicine Bow Mountains (MBM) in southeast Wyoming, USA (Figure 1). This range is lower and narrower (in the cross-wind direction) than the Sierra Nevada or the Rocky Mountain Front Range, but like those ranges it is asymmetric, with a steeper lee side than the windward side. Recent observational [21] and modeling [22] studies focused on boundary layer separation, rotor formation and wave breaking in the lee of the MBM. French et al. [21] used the same aircraft and airborne radar as used herein (i.e., the Wyoming Cloud Radar or WCR), but their observations are relatively limited since they lacked radiosonde data on the windward side and were collected in a brief period. This brief period of data collection was sufficient to capture rapid dynamic evolution of the downslope windstorm [21]. A follow-up study by Strauss et al. [23] analyzed WCR and flight-level vertical velocity data to quantify turbulence intensity (more specifically, the cubed root of the energy dissipation rate) in breaking mountain waves.

This study presents some unique high-resolution (~30 m) airborne radar observations of a downslope wind storm that persisted for at least five hours. The radar data are limited to two dimensions (the vertical plane), within the radar echo region, and provide kinematics only. Therefore we also use a 1 km resolution non-idealized numerical simulation of this event to place the radar observations in a dynamically consistent 4D context.

The primary objective of this study is to examine the fine-scale flow and turbulence structure of a downslope windstorm in the lee of the MBM. We also analyze upstream conditions in this and 19 other winter storms over the same mountains, to explore the predictability of cross-mountain flow acceleration and downslope wind formation based on upstream wind and stability profiles.

Observational and modeling designs are presented in Section 2. Section 3 provides an overview of atmospheric conditions of the downslope windstorm, based on soundings and WRF modeling. WCR observations are presented in Section 4. The question of predictability based on upstream stability and flow characteristics is discussed in Section 5. A summary follows in Section 6.

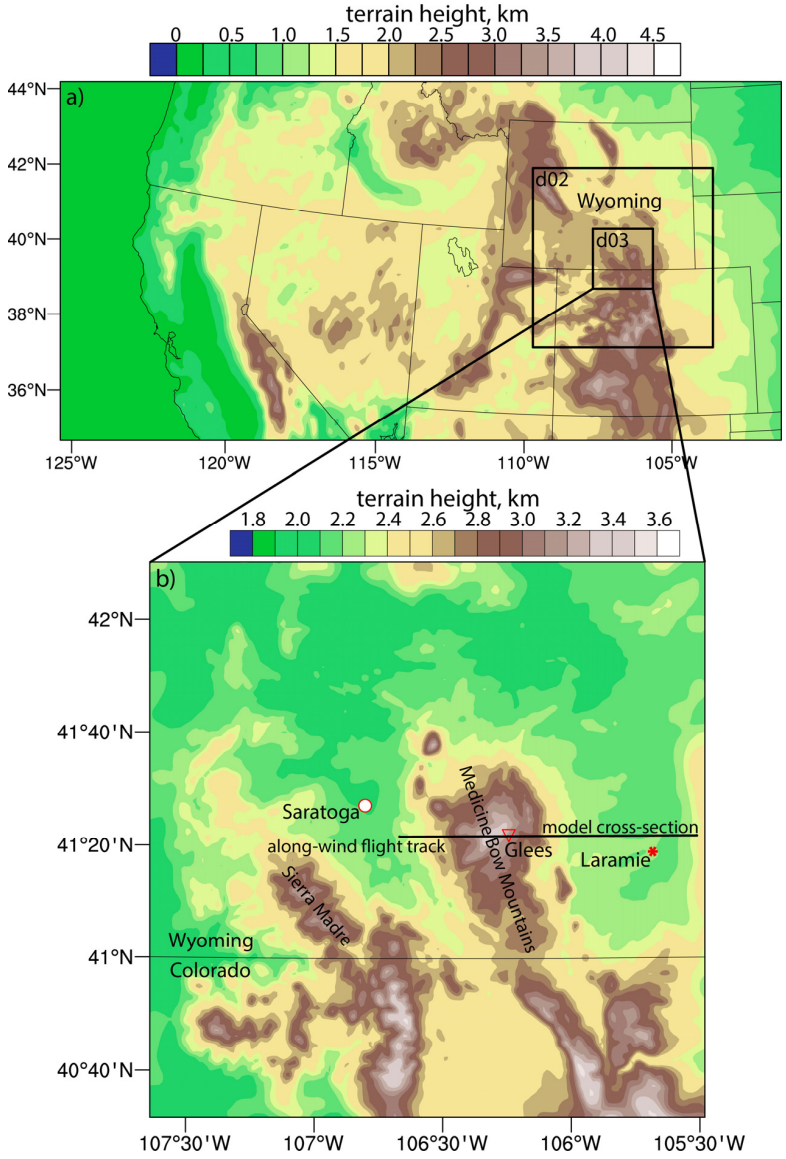


**Figure 1.** Terrain maps showing (**a**) the three WRF model domains (with coastline and state boundaries within the USA, and (**b**) the inner domain showing the model cross section and surface sites. The four UWKA flight tracks were along the model cross-section, but were shorter, ranging from 30 to 60 km in length.

## 2. Observational and Modeling Design

### *2.1. Instruments*

This study uses data collected on 11 January 2013 during the AgI Seeding Cloud Impact Investigation (ASCII-13) field campaign [24]. This campaign was not intended to study mountain waves or downslope wind storms. If it was, many more transects across the wind storm would have been flown, over longer distances and a different flight levels. In any event, the data presented here illustrate an impressive, persistent downslope wind storm event encountered by chance. The University of Wyoming King Air (UWKA) conducted two flights over the MBM (Figure 1b) on 11 January 2013, and three rawinsondes were launched from Saratoga (Figure 1b), upstream of the MBM. No radiosondes were launched from downstream locations, but aircraft soundings were collected some 30 km downstream of the MBM, between 4.2 km MSL and the airport in Laramie (2.2 km MSL).

The UWKA carried the WCR, a 3-mm (95 GHz) Doppler radar with fixed antennas oriented in various directions. Here we use three antennas: one pointing up (zenith beam), one down (nadir beam), and 30° forward of nadir (down-forward beam). The beam widths of these antennas ranges from 0.5° to 0.7° and the pulse width during this flight was 37.5 m, although data were sampled at 15 m range resolution. WCR profiles were sampled at about 20 Hz, which corresponds to an along-track resolution of 4–5 m at typical UWKA airspeeds of 80–100 $m \cdot s^{-1}$. The minimum detectable (radar equivalent) reflectivity for the most (least) sensitive WCR beam was about –33 (–28) dBZ at a range of 1 km, and the maximum unambiguous radial velocity was $\pm 15.8$ $m \cdot s^{-1}$ on this flight. Reflectivity values generally were quite low in the downslope wind storm examined here. They were highest on the windward side, but even there they did not exceed 10 dBZ as the storm was rather shallow and produced only light snowfall. This snow sublimated quickly on the lee side, but WCR echoes persisted remarkably long on the lee side, due to a mixture of sublimating ice particles and blowing snow particles. The latter result from strong winds scouring the surface and lofting the saltating ice particles into the turbulent boundary layer [25].

In the absence of deviations from aircraft reference pitch and zero roll, the radial velocity obtained from the up and down beams represents the vertical velocity of the reflectivity-weighted hydrometeors. However, aircraft wobble during flight, especially in turbulent areas, causes these radial velocities to become contaminated by both the aircraft motion and the horizontal winds. The effects of aircraft motion are automatically removed during post-processing, but horizontal wind contamination must be corrected for separately by assuming some horizontal wind profile. For lack of sounding data, French et al. [21] used instantaneous flight-level winds (assumed to be constant down to the ground) for this wind profile. Here the Saratoga radiosonde nearest in time to the flight pass is used for this wind profile. As will be shown later, the wind profile changes dramatically across the MBM crest. This change is not accounted for, and results in higher uncertainty in vertical velocity estimation, especially where the aircraft attitude variations (pitch and roll) are large.

The resulting hydrometeor vertical velocity is the sum of the air vertical velocity and the (negative) hydrometeor fallspeed. The latter is not estimated, but WCR vertical velocity will be displayed using a color scheme centered at –1 $m \cdot s^{-1}$, such that positive (negative) values can be interpreted as air updrafts (downdrafts). A fallspeed estimate of 1 $m \cdot s^{-1}$ is reasonable for unrimed snow (e.g., [26,27]), although it may be high for blowing snow particles [25]. In any event, the actual fallspeed is small compared to observed WCR vertical velocities in the downslope wind storm and hydraulic jump, as will be shown below.

Radial velocities from the two downward-pointing WCR beams, which are ~30° apart, are utilized to obtain the 2D wind field in a quasi-vertical plane below the aircraft. For flight legs that are oriented across the MBM, roughly along the wind, this allows for examination of the downslope wind storm and leeside flow phenomena. Damiani and Haimov [28] describe the details of the technique for vertical-plane dual-Doppler synthesis. This technique, used here, has been used in many other WCR-focused studies, including Geerts et al. [29–31], Yang and Geerts [32], Miao and Geerts [33], Sipprell and Geerts [34], Damiani et al. [35], French et al. [21], and Bergmaier and Geerts [36]. Close alignment of the flight track along the flight-level wind (as is the case in the event examined here) minimizes the difference between the aircraft heading and track angles, a difference that may be large when the cross-track wind is strong. An along-wind flight track ensures close alignment of the nadir and down-forward beams, and reduces the uncertainties in the dual-Doppler synthesis [28].

In addition to the WCR, the UWKA carried a backscatter lidar, the Wyoming Cloud Lidar, and several in situ probes to measure temperature, humidity, 3D wind, eddy dissipation rate (EDR), and cloud physics (including a Cloud Droplet Probe and two 2D optical array probes).

The UWKA made four along-wind passes during two flights over the MBM. Data were collected in all four transects on the upstream and downstream sides of the MBM; however, for one of the passes the WCR failed in intense turbulence on the lee side.

### *2.2. Numerical Model Setup*

To place the WCR observations in a dynamically consistent 3D context that is continuous in time and is not limited to the area of radar echoes, we ran a WRF simulation at 1 km resolution. The WRF model output will be used to examine the evolution of the downslope wind storm and the vertical structure of the atmosphere over a domain much larger than the domain of the flight tracks. Here we use WRF version 3.7.1 [37]. Three nested domains are used, with horizontal grid spacing ($\Delta x = \Delta y$) of 9 km (d01), 3 km (d02), and 1 km (d03) (Figure 1a). The model uses 61 terrain-following vertical levels in all three domains. The vertical grid spacing is about 19 m near the surface and increases roughly exponentially with height, but remains less than 200 m below 2 km above ground level (AGL).

The North American Model (NAM) reanalysis, available at three-hourly intervals with 12 km resolution, was used to drive the model's initial and boundary conditions. Fluxes in the PBL are parameterized with the Mellor–Yamada–Janjić scheme (MYJ, [38]), while horizontal diffusion is handled with a Smagorinsky first-order closure scheme (Table 1). The WSM 6-class graupel scheme [39] is used for cloud microphysical processes and atmospheric radiation is treated with the RRTM scheme [40] for longwave radiation and the Dudhia [41] scheme for shortwave radiation. The simulation was initialized at 0000 UTC on 11 January 2013 and carried forward for 30 h. The first few hours of the run are regarded as spinup time and the model output data are analyzed from 1800 UTC of 11 January to 0400 UTC of 12 January, matching the observational period. Only inner domain (d03) model data are analyzed here. The WRF data will first be validated against independent radiosonde data, and then will be used to describe the downslope wind storm and terrain induced gravity waves, as seen in a $\Delta x = 1$ km simulation.

**Table 1.** WRF model configuration and domains used in this study.

| Domains: $\Delta x = \Delta y$ | d01: 9 km | d02: 3 km | d03: 1 km |
|---|---|---|---|
| Simulation time | 30 h starting on 11 January 2013 at 00 UTC | | |
| grid points | 241 × 121 | 181 × 181 | 181 × 181 |
| time steps (seconds) | 30 | 10 | 3.3 |
| driver | 12 km NAM | nested | nested |
| vertical level | | 60 layers | |
| PBL and Turbulence | MYJ scheme [38] and Horizontal Smagorinsky first-order closure | | |
| SW radiation | Dudhia scheme [41] | | |
| LW radiation | RRTM scheme [40] | | |
| land surface | Noah land-surface Model | | |
| microphysics | WSM 6-class graupel scheme [39] | | |

## 3. Atmospheric Conditions

### *3.1. Synoptic Conditions*

At 00 UTC on 12 January 2013, about the middle of the UWKA flight period, the MBM region in southern Wyoming was in a cold airmass, with a low tropopause overhead. A deep upper-level trough was present to the southwest of the MBM, with a closed circulation at all levels up to 300 hPa, and a strong southwesterly 300 hPa jet across the Great Plains (Figure 2a). The 500 hPa flow was rather weak in the cold airmass over the MBM region, with several weak vortices evident in the NAM data (Figure 2b). The low-level cold-frontal trough was well east of the MBM, extending from eastern North Dakota to eastern Colorado (Figure 2c). At the surface, the cold-frontal trough was further to the east, e.g., in southeastern Nebraska, and was followed by cold-air advection across the northern Great Plains (Figure 2d). The wind in the MBM area was generally westerly from the surface to 300 hPa, slightly backing with height (Figure 2), except for the 400 hPa level, where the flow was weak from the southeast (not shown). At ~30 knots, the 700 mb (near MBM crest level) westerly flow in the MBM area was not exceptionally strong (Figure 2c).

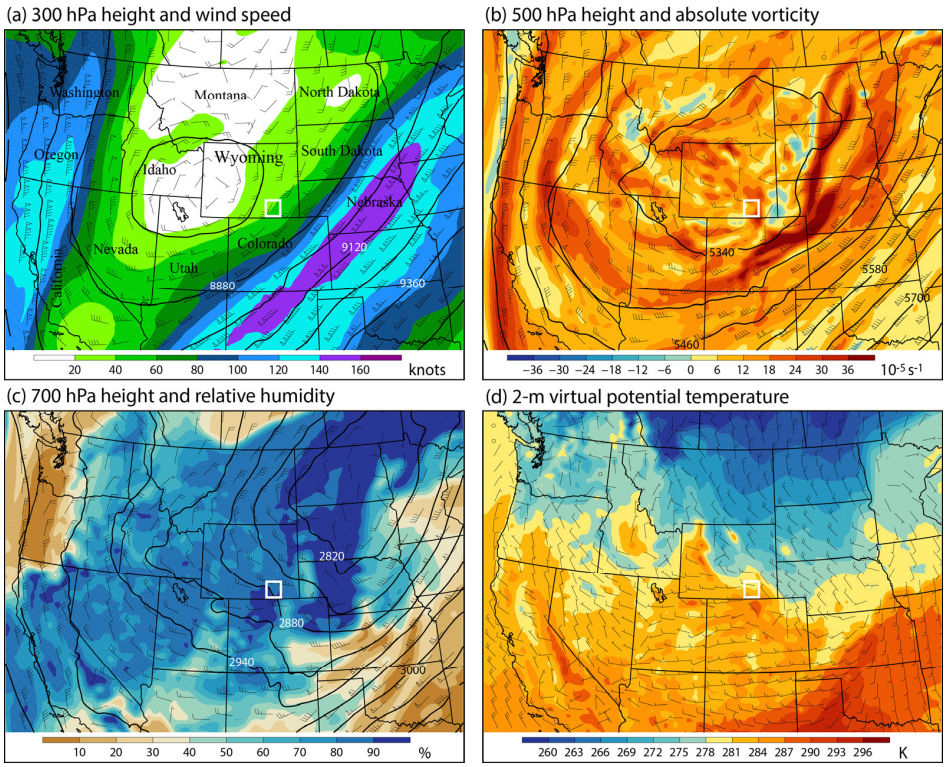


**Figure 2.** Synoptic condition from the 12 km NAM data at 0000 UTC on 12 January 2013. Wind barbs (full barb = 10 knots) are shown at each level, including at the surface (10 m) in (**d**). The white box in each panel shows the location of the Medicine Bow Mountains.

### *3.2. Upstream Vertical Profile*

Three soundings were released from Saratoga (Figure 1), upstream of the MBM, within three- to five-hour intervals. The elevations of Saratoga and MBM peak are about 2060 and 3661 m MSL, respectively, and the horizontal distance between these two locations is 42 km. A lower mountain range, the Sierra Madres southwest of Saratoga, should also be noted. The second sounding was released just before the first UWKA flight, and the last sounding was released near the end of the second UWKA flight. These soundings reveal the change in atmospheric vertical structure during an eight-hour period. The reasons we discuss the first two soundings (before the UWKA flight) are (a) that it takes some time (roughly one hour) for conditions over Saratoga to be advected to the lee side of the MBM, (b) that earlier conditions may have been essential to the formation of a breaking wave, which then may have become somewhat self-sustaining through a self-induced critical level, and (c) the model produced a high-amplitude non-linear wave at an earlier time, before the UWKA observation period.

The first sounding, released at 17:00 UTC (10 am local time), reveals a well-mixed, windy boundary layer (below 2.4 km MSL) capped by a weak inversion at ~2.8 km MSL (Figure 3a,d). The wind steadily backed from near the surface up to 6 km MSL (Figure 3e,f). Rapid backing occurred across a stable layer between 5.5–6.1 km MSL with southeasterly wind above this stable layer. Such reversal of the cross-barrier flow, from low-level westerly wind to (south)easterly wind starting about 2 km above the MBM crest, may be important, as it may support downslope wind storm formation [16,42]. The wind reversal level is referred to as a critical level, as the phase speed of orographic internal gravity waves is zero.

The stability of this critical level increases dramatically in the next three hours (compare the first to the second sounding in Figure 3d). Significant cooling occurred below this elevated inversion in those three hours. The well-mixed boundary layer was deeper (~1.2 km deep), probably on account of

the cold-air advection, but otherwise the fundamental vertical structure remains unchanged from three hours earlier. The third sounding seven hours later (Figure 3c) is, however, fundamentally different from the first two soundings: the elevated inversion layer (~5.5–6.1 km MSL) and the southeasterly flow above it are absent, and cloudiness probably occurred up to the (very low) tropopause (Figure 3c). The temperature was also lower below the (vanished) elevated inversion layer, but only slightly, compared to seven hours earlier. The low-level westerly wind remained equally strong, ~15 m·s$^{-1}$.

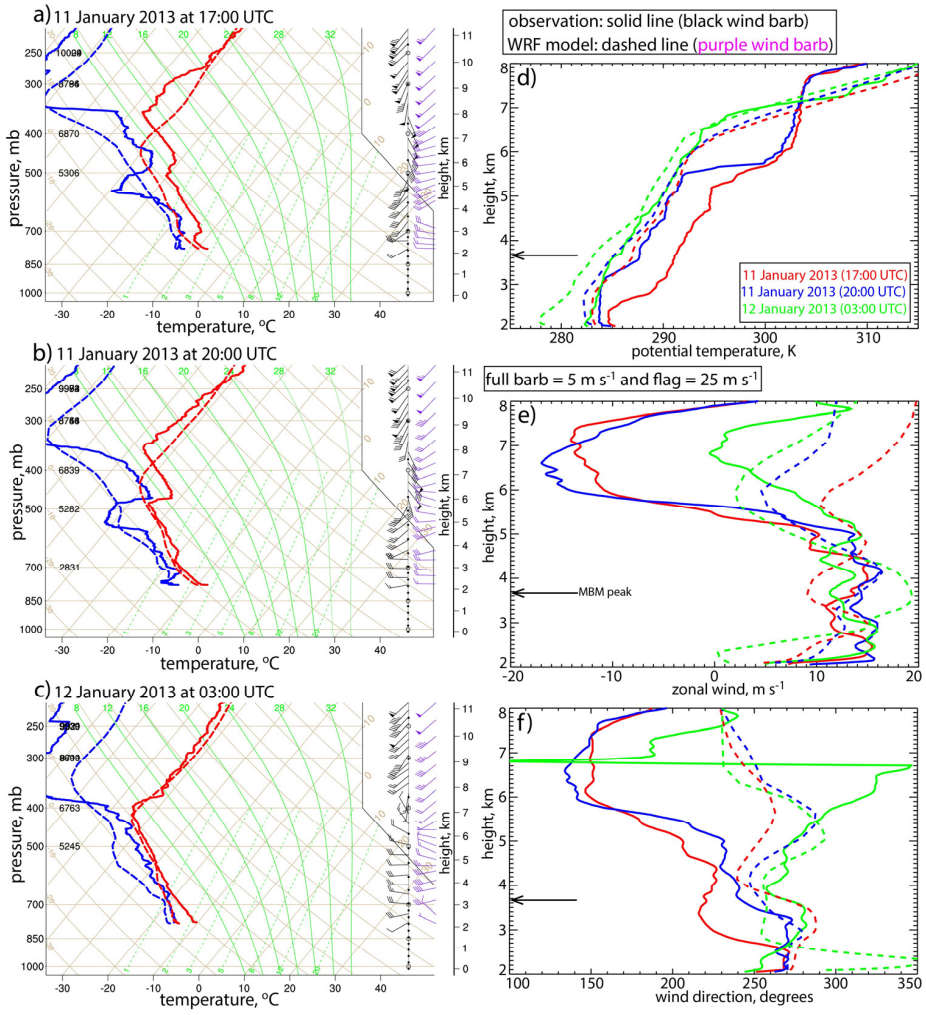


**Figure 3.** Vertical profile of the upstream atmosphere, at Saratoga, according to radiosonde data (solid lines) and the inner-domain WRF model (dashed lines). The first three panels (**a**–**c**) show temperature (red lines) and dewpoint (blue lines) on a skew T diagram, with wind barbs on the side (full barb = 5 m·s$^{-1}$ and flag = 25 m·s$^{-1}$), at three different times. Panels (**d**–**f**) show the vertical profiles of potential temperature, zonal wind speed, and wind direction, respectively. The height of Medicine Bow Peak is marked by a black arrow in the last three panels.

Markowski and Richardson [10] list seven conditions conducive to downslope wind storms: (a) a high, asymmetric mountain with a steeper lee slope; (b) strong cross-barrier winds (>15 m·s$^{-1}$) at and just above mountaintop level; (c) the wind at this level should be close to normal to the barrier (within 30°); (d) a stable layer near or just above mountaintop level, and a less stable layer above; (e) cold-air advection and large-scale subsidence to reinforce this stability structure; (f) reverse wind shear and a critical level aloft; and (g) the lack of a cold pool in the lee valley, which may inhibit the downslope storm from penetrating to the surface. In addition, the mountain half-width cannot be so small that the advection time scale is shorter than a buoyancy period; otherwise the mountain cannot

generate a vertically propagating gravity wave response. The MBM is definitively wide enough in this case.

The first condition applies to the MBM. Other than this first condition, the six other conditions may not all be necessary. One could also question whether Saratoga, at ~one mountain width to the west of the MBM, is a representative upstream location. Further, it is not clear whether stronger conditions (e.g., stronger low-level wind, higher low-level stability) imply a stronger downslope windstorm. Thus, these conditions are evaluated qualitatively only.

In general these six conditions applied (although condition (b) only marginally) early in the UWKA observation period, i.e. for the second sounding, at 20:00 UTC. At this time (g) applied as well, with Laramie (located in the downwind valley, see Figure 1) reporting strong westerly winds and relatively high potential temperature, 287 K (Figure 4), 3 K higher than the potential temperature in the upwind well-mixed layer at 20:00 UTC (Figure 3d). This implies that potentially warmer air was mixed down into the lee-side airmass, i.e., the downslope wind storm reached the downwind valley. But Laramie experienced cooling after 20 UTC, as colder air moved in from the north (Figure 4). During most of the remainder of the UWKA flights the downslope windstorm may not have reached Laramie some 30 km downwind of the MBM, but it may have penetrated into the valley further west.

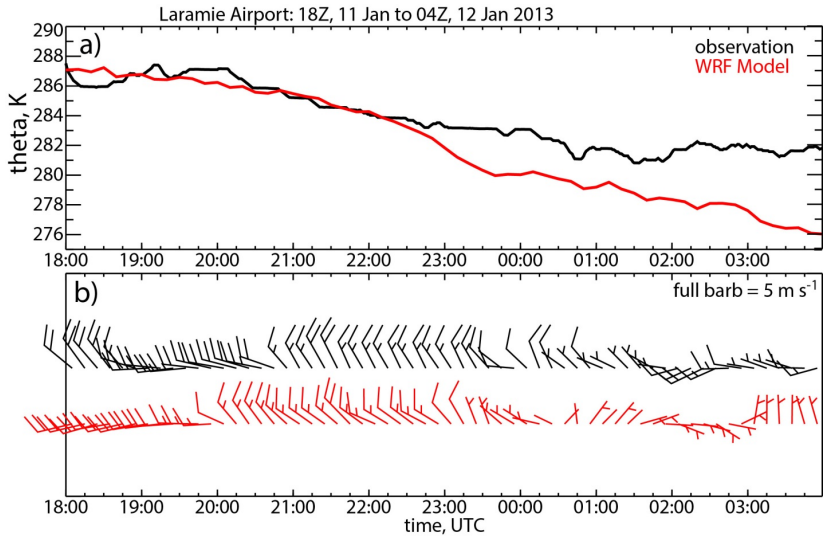


**Figure 4.** Comparison of surface observations (**black**) against WRF model (**red**) for (**a**) potential temperature and (**b**) wind. The model is compared against observations from the Laramie Regional Airport weather station during a 10-hour period on 11–12 January 2013.

Towards the end of the UWKA observation period, at 03:00 UTC (next day), conditions (d), (e), and (f) no longer applied [maybe (f) marginally did apply as the zonal wind did just reach 0 $m \cdot s^{-1}$ aloft], and condition (g) could not be verified. Most significant is condition (d), the lack of a stable layer near mountaintop level, below a less stable layer (Figure 3d). So conditions were less suitable for a downslope windstorm at 03:00 UTC. Yet at this time (around 03 UTC) the downslope wind storm was most intense, as will be shown below. It is possible that Saratoga was not a suitable upstream location, as it may have been affected by flow modified by the Sierra Madres, to the southwest of Saratoga (Figure 1b). This range also is rather asymmetric (condition a) and may produce downslope wind storms [43], although there is no evidence this happened on 11–12 January 2013. It is possible also that the downslope windstorm, triggered by suitable upstream conditions earlier on, somehow became self-sustaining by a self-induced critical level.

The WRF-simulated upstream conditions, in the inner domain (d03), are compared against radiosonde data in Figure 3. The WRF model "knows" about the Sierra Madres and should be able to capture their effect on low-level flow and stability above Saratoga. These low-level conditions (below

mountaintop level) are summarized in Table 2. The bulk Brunt–Vaisala frequency $N$ in Table 2 is calculated from the surface to mountaintop level, as a weighted mean of the dry value from the surface to the lifting condensation level (LCL) and the moist value above the LCL, the latter using the equation in [44]. Its average value ($N$ ~0.0073 $s^{-1}$) from three soundings compares very well with the time-space matched WRF value ($N$ ~0.0074 $s^{-1}$) (Table 2). This $N$ and the surface-to-mountaintop mean wind speed $U$ are used to compute the non-dimensional mountain height $h$ [$h = NH/U$, where H is the height of the mountain above the upwind plains]. For the first sounding, the modeled and observed $h$ values are close to 1, but for the other two soundings, the observed $h$ becomes smaller than 1 (suggesting unblocked flow), while the modeled $h$ becomes larger than 1 (suggesting more blocked flow). High $h$ values tend to imply higher-amplitude gravity waves and more significant departures from linear behavior in stratified flow (p. 14 in [45]). The high $h$ values in the model are due to an underestimation of the low-level wind speed in the last two soundings (Table 2). That in turn may be related to the fact that the modeled flow over Saratoga is less affected by the Sierra Madres: at 03:00 UTC, the observed low-level flow is from 271° and thus downwind of the northern part of the Sierra Madres, while the modeled wind is from 301° (Figure 3c,f), a direction lacking significant upwind terrain (Figure 1b). Other discrepancies in the WRF simulations, compared to radiosonde data, include excessively cold conditions in the first sounding (before the UWKA observations), suggesting that the model advected the colder airmass too early, and the lower tropopause than observed.

**Table 2.** Characterization of the upwind environment, and evaluation of model performance. Shown are the wind speed $U$, wind direction, the Brunt–Väisälä frequency $N$, and the Froude number $Fr$. All observations (OBS) are derived from a radiosondes released in Saratoga and model output is time–space-matched to these observations. Here $N$ is the depth-weighted average dry (moist) value of the Brunt–Väisälä frequency below (above) cloud base (defined as the LCL). The non-dimensional mountain height $h$ is calculated as $\frac{NH}{U}$ where $H$ is the height of Medicine Bow Peak (3,661 m MSL) above Saratoga (2070 m MSL). All variables are averages between the surface (10 m) and mountaintop level.

| Sounding Launch | | Average Value from Surface to Mountaintop | | | | | | | |
|---|---|---|---|---|---|---|---|---|---|
| Date | Time (UTC) | U (m/s) | | Wind Dir (°) | | N (0.01 $s^{-1}$) | | $h$ | |
| | | obs | model | obs | model | obs | model | obs | model |
| 11 January 2013 | 1700 | 16.7 | 10.1 | 240 | 277 | 1.06 | 0.54 | 1.03 | 0.85 |
| 11 January 2013 | 2000 | 14.9 | 10.9 | 265 | 270 | 0.57 | 0.67 | 0.57 | 0.96 |
| 12 January 2013 | 0300 | 14 | 8.2 | 271 | 301 | 0.55 | 1.02 | 0.59 | 1.96 |
| Average | | 15.2 | 9.7 | 259 | 283 | 0.73 | 0.74 | 0.68 | 1.10 |

The main model discrepancy is the lack of elevated inversion (around 5.5–6.1 km MSL) and the concomitant lack of wind reversal in the upper troposphere in all three soundings (Figure 3). The latter is one of the seven conditions for downslope windstorms mentioned before. While condition (f) is not satisfied in the model, conditions (b) [regarding cross-MBM wind speed] and (d) [regarding change of stratification with height] are satisfied more convincingly in the last two model soundings (during UWKA observations) (Figure 3). Thus upstream conditions in the WRF simulation appear conducive to a downslope windstorm throughout the 10-hour period, except for the lack of a critical level and significant reverse shear (condition f).

### *3.3. Modeled Flow Field across the Mountain*

Vertical cross sections of vertical velocity, potential temperature, and horizontal wind are shown in Figure 5, for a 10-hour period (from 18 UTC Jan 11 to 04 UTC 12 January 2013), the last five of which overlap with the UWKA transects. These zonal cross sections are obtained from the innermost domain along the line in Figure 1b, which transects the top of the MBM and matches the UWKA flight track. The zonal wind for the corresponding model transects is shown in Figure 6.

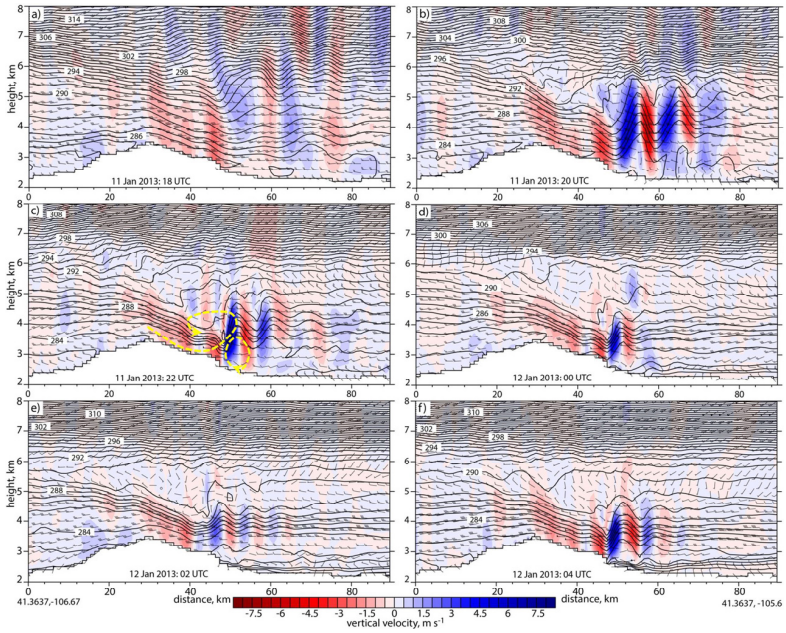


**Figure 5.** Model vertical cross sections of vertical velocity (color filled), potential temperature (black lines), and wind vectors along the transect line shown in Figure 1, from west to east, at two-hour increments starting in panel (**a**) at 18:00 UTC on 11 January. Two counter-rotating vortices (yellow dashed lines) are shown schematically in panel (**c**).

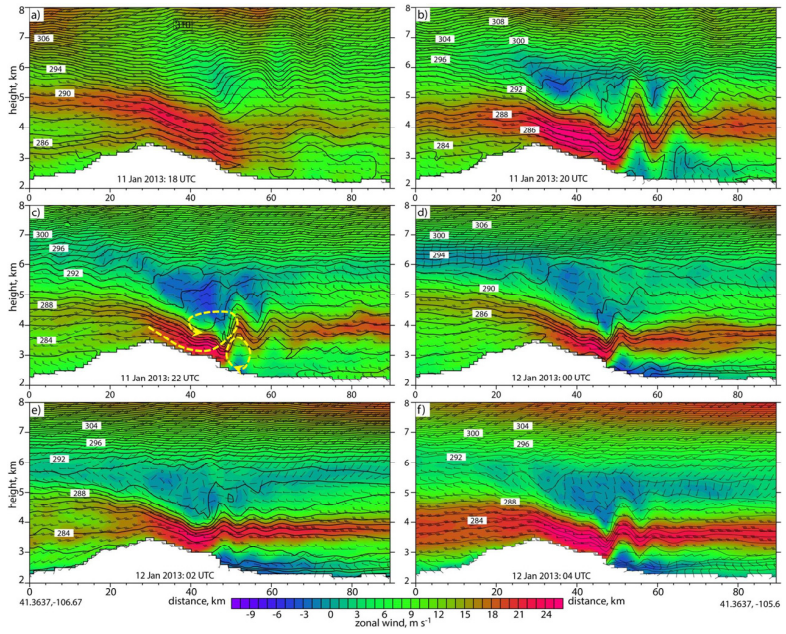


**Figure 6.** As in Figure 5, but showing zonal wind speed.

Lee gravity waves are present as early as 18 UTC (Figure 5a), and high amplitude trapped lee waves can be seen at 20 UTC (Figure 5b). A deep isentropic layer resulting from a dividing streamline [3] starts to develop over the MBM at 22 UTC (Figure 5c), near 5 km MSL. The upstream stratified air plunges down below this isentropic layer, especially at 22 UTC when this plunging flow transitions to an updraft (hydraulic jump) reaching 8 m $s^{-1}$ (at x = 52 km in Figure 5c). This subsiding, near-surface flow reaches a speed of 25 m $s^{-1}$ some 15 km downwind of the crest (Figure 6c). This speed is twice as large as the upstream wind speed. Two vortices flank the hydraulic jump at 22 UTC, both with an

easterly flow component. These vortices are drawn schematically in Figures 5c and 6c. Trapped lee waves persist for some distance further downwind. The amplitude of the wind storm is suppressed at 00 UTC and 02 UTC (Figure 5d,e), but is larger again, although more shallow, at 04 UTC (Figure 5f).

Transects of model turbulent kinetic energy (TKE, $m^2$ $s^{-2}$) and eddy dissipation rate (EDR, $m^{2/3}$ $s^{-1}$) are shown in Figure 7, valid for 20 UTC, a time when the downslope windstorm and hydraulic jump are best developed. We would like to estimate EDR from model output, because EDR is a well-established measure of the subjective feel of turbulence experienced by aircraft passengers. EDR values for specific-size aircraft are linked to turbulence severity categories in pilot reports. There is no physically based relationship between TKE and EDR. Especially for smaller aircraft, EDR values are affected mostly by kinetic energy at the smaller scales of the inertial subrange. Here, the EDR is estimated using an experimental equation (1) proposed in Regmi et al. [46] for an aircraft of similar size to the one used in this study:

$$EDR = \left[ 0.238 \times \frac{(TKE - 0.1)^{\frac{3}{2}}}{L_E} \right]^{\frac{1}{3}} \quad (1)$$

where $L_E$ (m) is the length scale. Model estimations of TKE and $L_E$ are based on the MYJ PBL parameterization (Table 1). (Model EDR is shown here because it is a standard measure of turbulence intensity experienced aboard an aircraft, and it also directly measured at flight level, see below.) High TKE and EDR values at 20 UTC (Figure 7) flank the highly stratified plunging jet (Figure 6b) both above and below, highlighting shear as a key source of TKE. They further flank the hydraulic jump (ascending isentropes). However, TKE and EDR values are especially high just downstream of the hydraulic jump, in the rotor.

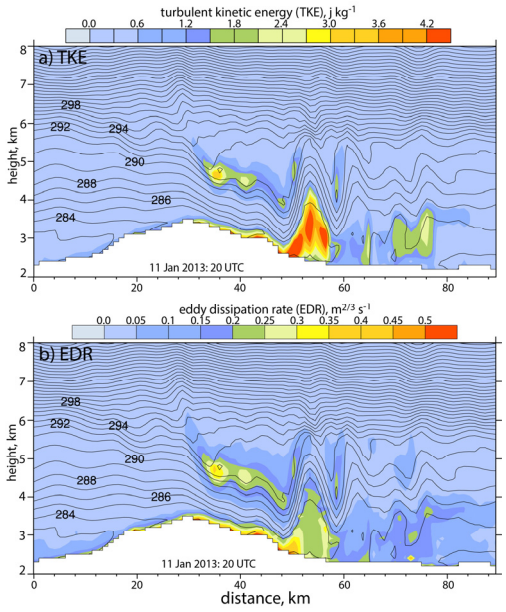


**Figure 7.** Model vertical cross sections of (**a**) TKE and (**b**) the EDR at 20:00 UTC on 11 January 2013. The black lines in both panels are the potential temperature.

Notwithstanding some discrepancies between modeled and observed upwind stratification and wind profile (Section 3.2), the WRF simulation captures an evolving downslope windstorm with, at times, a hydraulic jump just upwind of the downstream valley, counter-rotating vortices, a breaking wave, and residual trapped lee waves. One discrepancy with observations presented so far is the penetration of a colder airmass from the north in the lee valley after 22 UTC (Figure 5). The resulting

cooling in Laramie (Figure 1) is inconsistent with observations (Figure 4). This cold pool may prevent deeper penetration of the plunging flow into the Laramie valley [condition (g) in Section 3.2].

## 4. Radar Observations of the Downslope Wind Storm and Turbulence

### *4.1. Reflectivity*

The 20 UTC sounding reveals moist layers at low levels and near 6 km MSL (Figure 3b), while the 03 UTC sounding reveals rather moist conditions up to the tropopause, mainly between 3 and 6 km MSL. Both soundings support stratiform orographic clouds and precipitation. The structure and evolution of radar echoes across the MBM (Figure 8) can be interpreted in this context. The four WCR reflectivity transects collected on an along-wind flight track over a 5.2-hour period are shown in Figure 8. This track aligns exactly from west to east, and coincides with the model transects (Figures 5 and 6); however, the length of the flight tracks varies. The direction of the flight is either from east to west or west to east, as shown by an arrow in each panel, but the west (upwind) side is always plotted on the left side. These transects cover both sides of the crest except the third panel (Figure 8c), for which no WCR data were available on the lee side.

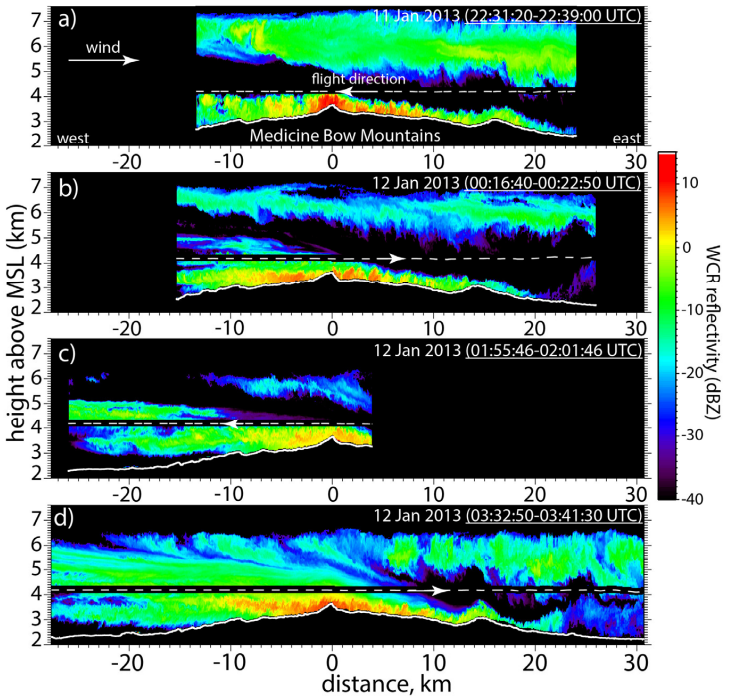


**Figure 8.** WCR-measured radar reflectivity for the four along-wind transects over the MBM flown over a five-hour period starting, in panel (**a**), at 22:30 UTC on 11 January 2013. The actual flight times are shown in the plots. The dashed line and arrow in all panels show the flight level and flight direction, respectively. The black belt centered at flight level is the radar blind zone. Distance 0 km in all panels corresponds with the crest of the MBM and the largest distance from panel (**d**) is kept in all panels.

Shallow, stratiform clouds formed upwind of the MBM, producing light snowfall mainly over the crest (Figure 8). Snowfall extended into the lee, close to the ground. The somewhat cumuliform echoes in the lee, near the surface, are attributed to intense turbulence, as will be shown below. The echo strength and depth decreased with distance from the crest and sublimating falling snow likely transitioned to blowing snow further leeward, although WCR data do not allow for a distinction between the two types of snow. A cirrostratus layer aloft, likely advected from the south (Figure 3b), remained decoupled from the shallow orographic cloud (Figure 8). It weakened from the first to the third WCR transect. In the last WCR transect a new cirrus layer, advected from the west and merged with the low-level cloud, was drawn into the plunging flow over the MBM (Figure 8d).

### *4.2. Flight-Level Measurements*

Measurements at flight level (~4.27 km MSL, or ~0.6 km above Medicine Bow Peak) for the same four UWKA passes are shown in Figure 9. As mentioned in Section 4a, all four passes do not cover the same distance; however, the position of the MBM crest is centered at 0 km (vertical dotted line) in all panels in Figure 9. (The underlying terrain profiles are shown in Figure 9e.) All four passes reveal a drastic change in temperature, vertical velocity, wind, and turbulence from the upwind side to the immediate lee of the crest. Potential temperature increased by as much as 7 K within 8–10 km behind the crest (Figure 9a), due to ~2 m·s$^{-1}$ subsidence (Figure 9b). This sinking flow also accelerated by 6–10 m·s$^{-1}$ (Figure 9c) but remained mostly laminar (Figure 9d), until it suddenly became turbulent about 8 km behind the crest. The region of lee turbulence contained downdrafts and updrafts ranging from −7 m·s$^{-1}$ to +12 m·s$^{-1}$ (Figure 9b), and locations where the zonal wind becomes slightly negative (easterly wind) (Figure 9c).

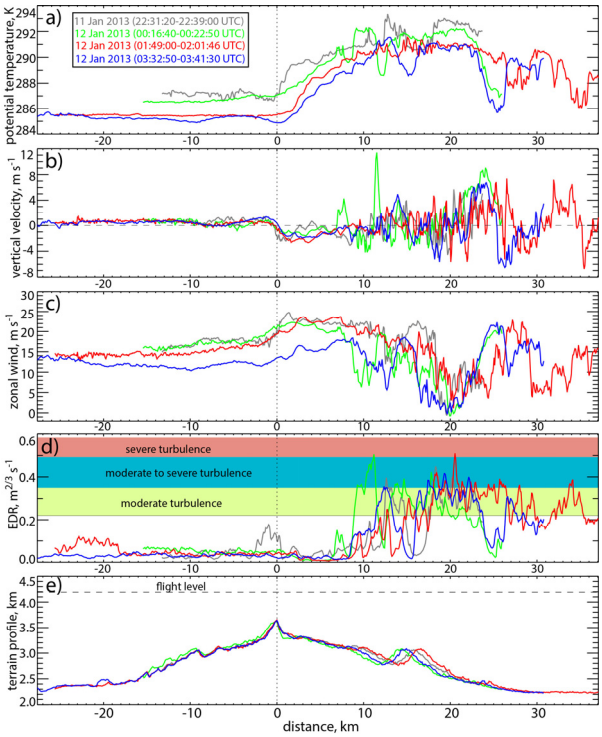


**Figure 9.** Flight-level atmospheric variables for the same four along-wind flight tracks shown in Figure 8. The vertical dotted line in all panels (x = 0) corresponds with the crest of the MBM. (**a**) Potential temperature; (**b**) vertical air velocity (the dashed line represents 0 m s$^{-1}$); (**c**) zonal wind; (**d**) eddy dissipation rate (EDR) measured by the MacCready turbulence meter, with colored layers indicating turbulence severity based on the classification of Strauss et al. [23]; and (**e**) underlying terrain profile (the dashed line in (**e**) represents the flight level).

Atmospheric turbulence at the flight level is evaluated using the EDR, measured by a MacCready Turbulence Probe [47]. The EDR measured by the MacCready Probe is proportional to the standard deviation of the vertical acceleration an aircraft experiences [48]. The MacCready EDR measurement has been adopted by the International Civil Aviation Organization as a measure of turbulence intensity in pilot reports. Measured EDR values are used to categorize the turbulence intensity at flight level. For medium-sized aircraft such as the one used in this study, EDR thresholds of 0.014, 0.050, 0.125, 0.220, 0.350, and 0.500 m$^{2/3}$ s$^{-1}$ refer to the turbulence categories 'smooth to light', 'light', 'light to moderate', 'moderate', 'moderate to severe', and 'severe' [23]. The latter three regions are highlighted in Figure 9d.

The UWKA experienced severe turbulence during the second and third passes and moderate to severe turbulence on the two other passes (Figure 9d). This indicates that moderate to severe turbulence was present for at least five hours in the lee of the MBM. The location and magnitude observed EDR values at flight level in all four transects ($0.2 < \text{EDR} < 0.4$ m$^{2/3}$ s$^{-1}$ about 10–30 km downwind of the crest) correspond well with those in the WRF simulation at the same level, but at an earlier time (Figure 7), although at 1 km resolution WRF cannot capture the observed fine-scale variability (Figure 9d). WRF simulated EDR values at times matching the flight transects are only one-third to one-half the observed values (not shown). It is challenging for a single numerical model run (driven by three-hour resolution reanalysis data in the outer domain) to realize the conjunction of conditions leading to wave breaking and downslope wind storm at precisely the right time [49,50].

The intense turbulence is consistent with remarkably high levels of TKE at flight level (Figure 10). Within the available spectral range, the power spectra of vertical velocity in the lee follow the $-5/3$ inertial subrange slope both near the ground and at flight level (Figure 10), thus within the ~30 km of lee-side stretch, small-scale vertical velocity variations (at a scale of less than a few km) are due to turbulence. WCR-based spectra can be produced up to 500 m AGL only, because of a lack of radar echoes at higher levels (Figure 8). This lack of radar echoes and the resulting noisy Doppler velocity field (with remaining velocity unfolding uncertainties) explain why we did not attempt to use WCR data to estimate the spatially resolved turbulence spectrum and EDR as in [23]. The spectral peak near 4–6 km in the last two transects in Figure 10 may be related to a hydraulic jump (see below). TKE tends to be higher at 500 m AGL than closer to the ground or at flight level. This is unlike typical shear-driven boundary-layer turbulence, which weakens with height in the boundary layer (e.g., [30]). It is also unlike the resolved turbulence in the WRF simulation, which generally weakens with height (Figure 7). The cause of this high TKE at 500 m AGL will become apparent in the next section.

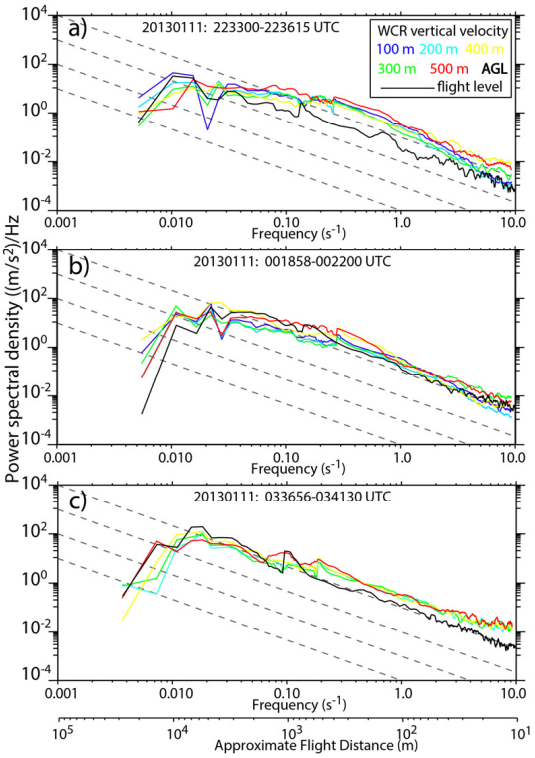


**Figure 10.** Power spectra of WCR vertical velocity (color lines, representing heights ranging from 100 to 500 m AGL) and flight-level vertical velocity (black line) for along-wind transect (**a**) #1, (**b**) #2, and (**c**) #4. Only the lee-side portion is included, a total distance of ~30 km. Frequency is converted to distance using the average ground-relative speed of the aircraft. The dashed lines show the –5/3 inertial subrange slope at increasing levels of TKE.

### *4.3. Vertical and Horizontal Wind below Flight Level*

The WCR measured vertical velocity is shown in Figure 11 for the four along-wind flight tracks. No data are available near the flight level due to the radar blind zone; that zone is partly filled with flight-level vertical air velocity data, which match well with the WCR vertical velocity. The zonal wind derived from WCR vertical-plane dual-Doppler is shown in Figure 12, below flight level only, together with the gust probe zonal wind plotted at flight level. The curved nature of that flight level in Figures 11 and 12, especially on the far lee side, is testimony to the strong vertical drafts the aircraft experienced, resulting in departures from assigned flight altitude. The hydrometeor streamlines in Figure 12 are defined as being tangential to the 2D hydrometeor velocity vectors, i.e. the vertical component includes the actual particle fallspeed, as in [28].

The flow over the windward side is weakly ascending and very smooth (the light-blue area, especially in Figure 11c). Terrain-driven vertical velocity dipoles are evident across the main crest and across a secondary crest in the lee. Turbulent rising and sinking eddies can be seen in the boundary layer, mainly in the lee, on account of the stronger winds there (Figure 12). Each transect shows a plunging, accelerating air current, starting above flight level just upwind of the crest and extending some distance in the lee, with wind speeds doubling to ~25 m·s$^{-1}$. In two transects, the second and the last ones, blowing snow is separated from the surface and lofted in a deep updraft reaching 8–9 m·s$^{-1}$ at flight level. This updraft occurred at x = 24 km downwind of the crest in both transects (Figure 11b,d). In the third transect, no WCR are available that far east, but a strong updraft and saturated (cloudy) air was encountered at x = 25 km (Figure 9b). This persistent updraft was deep, lifting the cirrus cloud base aloft (Figure 8b,d). This updraft, referred to as a hydraulic jump, was associated with the separation of the downslope windstorm from the boundary layer, implying strong low-level convergence (Figure 12b,d). The same hydraulic jump may have been present in the first transect, but the aircraft did not extend far enough leeward.

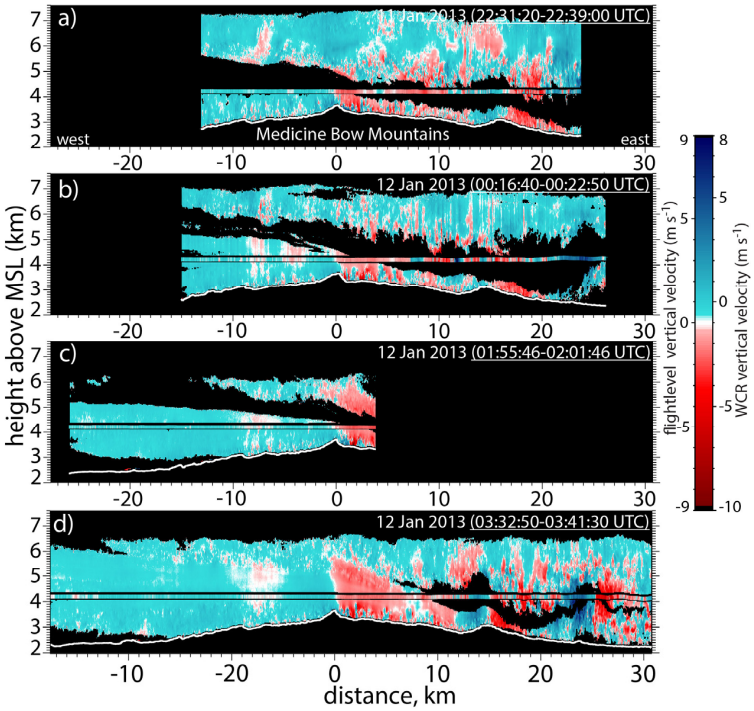


**Figure 11.** As in Figure 8, but for WCR measured hydrometeor vertical velocity. Also shown, at flight level, is the gust probe vertical air velocity. Note that the color bar is centered at 0 m·s$^{-1}$ for the gust probe, yet at –1 m·s$^{-1}$ for the WCR. This is intended to allow for interpretation of WCR data as air vertical motion.

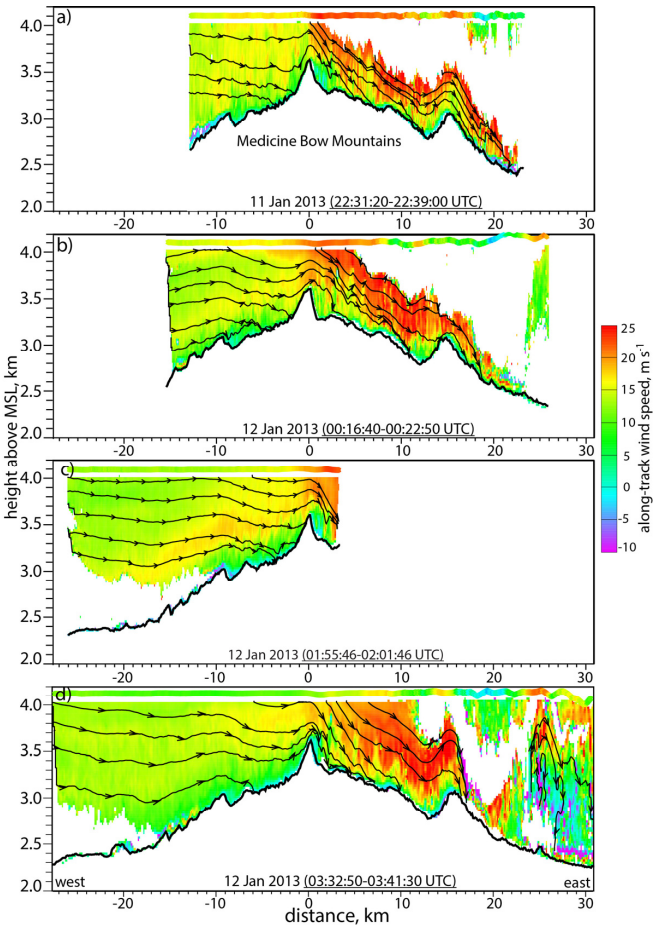


**Figure 12.** As in Figure 8, but for along-track (zonal) wind speed and hydrometeor streamlines, derived from WCR dual-Doppler synthesis. The gust probe zonal wind speed is shown at flight level.

### *4.4. Observation of a Rotor*

During the fourth and last flight track, which also was the longest and extended furthest east, the crew members experienced moderate to severe turbulence, both on the track shown here (Figure 9), and further downwind as the UWKA prepared for landing in Laramie. Figure 13 zooms in on the lee section of Figure 12d to examine the hydraulic jump and rotor. Snow particles were carried in the downslope wind storm, before being lofted at least 1 km, as the boundary layer separated from the surface and was drawn into the hydraulic jump, located around x = 24 km in Figure 13b. Unfortunately, no WCR echoes exist in the dry slot containing the core of the plunging current, but the zonal wind field (Figure 13c) suggests that the strongest mean wind occurred in that dry slot, between 500 and 1000 m AGL. The very strong shear near the edge of this jet invariably was unstable, resulting in intense turbulence that explains the very high TKE on the lee side just below this jet near 500 m AGL, as discussed in Section 4.2 (Figure 10). The same high turbulence, resulting from shear instability, can be seen near the top of the plunging current in the model (Figure 7).

The WCR echoes generally were very weak, near the minimum detectable signal level (~−30 dBZ) (Figure 13a), but the signal was strong enough to reveal a coherent, strong updraft (up to 10 $m \cdot s^{-1}$) extending to flight level (Figure 13b) and beyond. Two 3–4 km wide counter-rotating vortices on opposite sides of the hydraulic jump are drawn schematically in Figure 13c. Some (easterly) return flow can be seen both at flight level (near x = 20 km) and near the surface (near x = 27 km), although the dual-Doppler derived wind is less certain there due to the weak echoes and rapid aircraft attitude changes associated with the turbulence at flight level. The lower vortex, with vorticity pointing into

the page, is referred to commonly as a rotor. The two vortices in Figure 13c are similar to the ones highlighted in Figures 5c and 6c, although the modeled vortices are 2–3 times wider, presumably because of limitations associated with the model resolution.

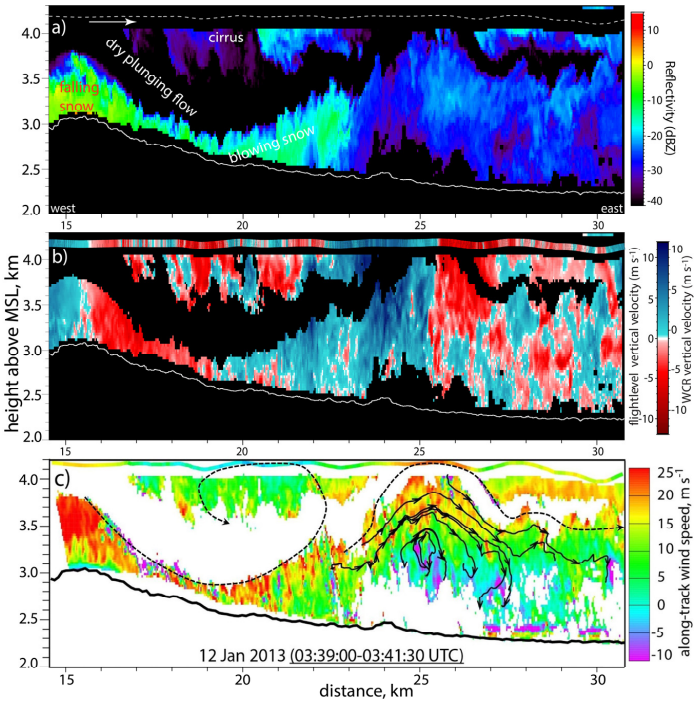


**Figure 13.** Zoomed-in view of the lee portion of the last WCR transect (distance matches with Figure 12d) highlighting the hydraulic jump and rotors. (**a**) Radar reflectivity; (**b**) hydrometeor vertical velocity; and (**c**) along-track wind speed with hydrometeor streamlines (solid lines) and schematically drawn counter-rotating vortices (dashed lines). The flight level is shown as a dashed line in (**a**), and flight-level vertical velocity and zonal wind speed are shown in (**b**) and (**c**), respectively.

## 5. Discussion

The persistent strong updraft seen in WCR data some 25 km downwind of the crest is referred to here as a hydraulic jump. The WCR transects are relatively short, and the radar echoes deteriorate with distance in the lee, for lack of scatterers. Thus, the data do not exclude the possibility that this updraft is part of a non-linear, high-amplitude trapped lee wave, as suggested by the WRF simulation. The transition from a trapped lee wave to a hydraulic jump is ill-defined, even in model output (e.g., [12]). Certainly, this wave involved a supercritical downslope flow that suddenly transitioned into a strong, deep updraft. Abundant turbulence was generated by the wave breaking in the hydraulic jump, but also by shear around the margins of the plunging jet.

Two counter-rotating vortices were observed and simulated as part of this strong updraft. Both observations and simulations show reverse flow in these vortices, at least in one of the transects. Turbulence near these vortices is not surprising given the tremendous wind shear associated with them. Hertenstein [19] and Hertenstein and Kuettner [20] describe two types of rotors, whose formation depend on the upstream environment: in both cases an inversion is present near mountaintop level, but the wind shear across this inversion varies. Under weak wind shear the rotor produces moderate or severe turbulence. Under stronger shear the rotor is associated with trapped lee waves, in which case the turbulence may be severe [4,20,22,51,52]. Both the WRF simulations and WCR observations suggest that the case presented here was predominantly of the second type.

This observational study adds to the growing body of literature describing the fine-scale structure of downslope wind storms and associated turbulence. While the MBM may be rather prone to

downslope wind storms [21,22,31], even under marginally strong wind at mountaintop level, they do occur elsewhere (as mentioned in the Introduction), including in more densely populated areas. Most severe wind events in the Boulder, Colorado area, for instance, are associated with downslope wind storms [53]. The present study builds on previous research over the MBM in Wyoming in that it documents the upwind conditions leading to a persistent downslope windstorm.

A better understanding of upstream conditions conducive to downslope wind storm formation should result in a better predictability of these potentially hazardous events. In the event studied here, the upstream conditions all appeared conducive initially, but later on several conditions no longer applied (Section 3.2), suggesting that the persistence of the downslope windstorm was affected by a self-induced critical level.

In an effort to evaluate predictability based on upstream conditions, we examined the cross-mountain acceleration and downslope windstorm formation in 19 other winter storms over the MBM. These storms were sampled by the UWKA with WCR in four different projects during the winters of 2006, 2008, 2009, and 2013. The cases were selected based on one other criterion, i.e., the availability of upwind vertical profile data, from aircraft soundings conducted near the Saratoga airport (in 2006) or radiosondes released from Saratoga during the UWKA flight. As in the present case study, the objective of those 19 flights did not relate to orographic wave dynamics, but rather to cloud microphysics, so they present a reasonable depiction of flow dynamics across the MBM in winter storms. In all 19 cases, at least one cross-mountain transect of horizontal wind derived from WCR dual Doppler synthesis was available. (In the 2008, 2009, and 2013 flights there were one or two per flight; in the 2006 flights, there were more.) In all flights the cross-mountain track was within 20° of east-west, and aligned to be normal to the low-level wind, which was close to westerly. We computed the average WCR along-track wind speed within 500 m AGL and within 10 km horizontal distance from the MBM crest, to obtain a mean upwind and mean leeside wind speed. We compute upwind stability as for Table 2, and upwind wind profile parameters are computed along the direction of the flight track.

Stronger winds in the lee (than the upwind side) are common, as predicted even by linear wave theory: they were observed in all but three cases (84%), but in most of these, the cross-crest acceleration was small. Significant acceleration across the crest (40% or higher increase in wind speed) occurred in just seven cases (37%). The wind increase in the 11–12 January 2013 case is rather larger (60% increase, on average for the three transects in Figure 12 with enough WCR data). There is no clear relationship between the cross-crest acceleration and different upstream conditions believed to be conducive to downslope windstorms (based on in Markowski and Richardson [10], see Section 3.2). Conditions (a) (mountain asymmetry, vertically propagating waves) and (c) (wind direction) were always satisfied, and conditions (e) and (g) are neither relevant nor assessable from an upwind sounding alone. The three remaining conditions mentioned in Section 3.2 are condition (b) (wind speed near mountaintop level), condition (d) (high stability at low levels and/or near mountaintop level, or decrease of stability from around mountaintop level to ~1 km higher), and condition (f) (a critical level aloft within the troposphere or reverse wind shear across mountaintop level). Scatterplots of mountaintop wind speed, stability (or change of stability with height), and wind shear (over various depths) against the leeside wind speed and against cross-crest acceleration ratio for these 19 cases (not shown) reveal that these sounding parameters offer little predictive value for downslope windstorms.

These findings should not be interpreted as implying that upstream conditions used by forecasters and stated in textbooks such as [10] are questionable. Rather, a single sounding at a fixed upstream location may not capture the relevant upstream conditions at the right time and place for specific mountain ranges. Given the non-linear nature of downslope windstorms, rotors, etc., upstream conditions at one time are not sufficient to predict them deterministically, as shown in [49,50]. Coarse-resolution operational weather prediction model output can be used to indicate general probabilities, but a more accurate (albeit computationally still prohibitively expensive) approach is to run an ensemble of simulations of sufficient resolution to resolve these phenomena. A 1-km resolution appears sufficient, at least in the case examined here.

## 6. Conclusions

This study describes a turbulent downslope wind storm and rotor event observed on 11–12 January 2013 in the lee of the MBM in southeastern Wyoming. The UWKA research aircraft made four passes along the low-level wind across the mountain during a five-hour period. The airborne measurements include a profiling radar able to map vertical and along-track wind in a vertical transect below flight level at a very fine resolution (~30 m). This case was numerically simulated using WRF at a resolution of 1 km. The following are the main findings:

- Even though the simulated vertical profiles of wind and stability departed somewhat from observed ones just upwind of the mountain range, with no critical level in the simulated wind profile, the model did produce supercritical wind in the lee, followed by a strong updraft flanked by counter-rotating vortices. This updraft had the appearance of a hydraulic jump and was followed by a decaying series of trapped lee waves. Intense turbulence was simulated near the plunging jet and the wave breaking area surrounding the hydraulic jump.
- WCR observations reveal persistent, intense cross-crest acceleration of the low-level flow, a plunging leeside jet separating from the boundary layer some 25 km downwind of the crest to produce a deep hydraulic jump (with updrafts up to 10 m $s^{-1}$) flanked by counter-rotating vortices, and (at least in one transect) a shallow rotor with reverse flow near the surface.
- Flight-level and WCR observations indicate persistent moderate to severe turbulence in the vicinity of the plunging jet and the wave breaking area.
- Upstream conditions were generally conducive to downslope windstorm formation, at least early on, before flight measurements. During the flight the critical level and the suitable stratification (more stable below, less stable above mountaintop) vanished upwind, suggesting that a self-induced critical level may have sustained the downslope windstorm.
- A sampling of 19 other winter storms over the same mountain range suggests that the predictability of downslope windstorms based on coincident upstream conditions alone is poor.

**Acknowledgments:** This research and the 11–12 January 2013 UWKA flight were funded by the National Science Foundation grant AGS-1058426.

**Author Contributions:** Binod Pokharel analyzed all data used in this study, led the WRF simulations, and wrote the paper. Xia Chu assisted with the WRF model output analysis and Philip Bergmaier assisted with the WCR dual-Doppler synthesis. Bart Geerts provided oversight of the project and the write-up.

**Conflicts of Interest:** The authors declare no conflict of interest.

## References

1. Lee, T.J.; Weaver, J.F.; Pielke, R.A. Numerical predictions and nowcasting of downslope windstorms along the Colorado Front Range, Preprints. In Proceedings of Fifth Conference on Mountain Meteorology, Boulder, CO, USA, 25–29 June 1990.
2. Cotton, W.R.; Weaver, J.F.; Beitler, B.A. An unusual summertime downslope wind event in Fort Collins, Colorado, on 3 July 1993. *Weather Forecast.* **1995**, *10*, 786–797. [CrossRef]
3. Clark, T.L.; Hall, W.D.; Kerr, R.M.; Middleton, D.; Radke, L.; Ralph, F.M.; Neiman, P.J.; Levinson, D. Origins of aircraft-damaging clear-air turbulence during the 9 December 1992 Colorado downslope windstorm: Numerical simulations and comparison with observations. *J. Atmos. Sci.* **2000**, *57*, 1105–1131. [CrossRef]
4. Ralph, F.M.; Neiman, P.J.; Levinson, T.L.; Fedor, L. Observations, simulations, and analysis of nonstationary trapped lee waves. *J. Atmos. Sci.* **1997**, *54*, 1308–1333. [CrossRef]
5. Smith, R.B. On severe downslope winds. *J. Atmos. Sci.* **1985**, *42*, 2597–2603. [CrossRef]
6. Van der Mescht, D.; Eloff, P.J. Mountain wave-induced rotors in the lee of the Hex River Mountains. *S. Afr. Geogr. J.* **2013**, *95*, 117–131. [CrossRef]
7. Kaplan, M.L.; Huffman, A.W.; Lux, K.M.; Charney, J.J.; Riordan, A.J.; Lin, Y.-L. Characterizing the severe turbulence environments associated with commercial aviation accidents. Part 1: A 44-case study synoptic observational analysis. *Meteorol. Atmos. Phys.* **2005**, *88*, 129–152. [CrossRef]

8. Grubišić, V.; Doyle, J.D.; Kuettner, J.; Dirks, R.; Cohn, S.A.; Pan, L.L.; Mobbs, S.; Smith, R.B.; Whiteman, C.D.; Czyzyk, S.; et al. The terrain-induced rotor experiment: A field campaign overview including observational highlights. *Bull. Am. Meteorol. Soc.* **2008**, *93*, 653–668. [CrossRef]
9. Lin, Y.-L. *Mesoscale. Dynamics*; Cambridge University Press: New York, NY, USA, 2007.
10. Markowski, P.; Richardson, Y. *Mesoscale Meteorology in Midlatitudes*; Wiley-Blackwell: San Francisco, CA, USA, 2010.
11. Long, R.R. Some aspects of the flow of stratified fluids. Part I: A theoretical investigation. *Tellus* **1953**, *5*, 42–58. [CrossRef]
12. Durran, D.R. Another look at downslope windstorms. Part I: The development of analogs of supercritical flow in an infinitely deep, continuously stratified fluid. *J. Atmos. Sci.* **1986**, *43*, 2527–2543. [CrossRef]
13. Clark, T.L.; Peltier, W.R. Critical level reflection and the resonant growth of nonlinear mountain waves. *J. Atmos. Sci.* **1984**, *41*, 3122–3134. [CrossRef]
14. Scinocca, J.F.; Peltier, W.R. The instability of long's stationary solution and the evolution toward severe downslope windstorm flow. Part I: Nested grid numerical simulations. *J. Atmos. Sci.* **1993**, *50*, 2245–2263. [CrossRef]
15. Wang, T.-A.; Lin, Y.-L. Wave Ducting in a stratified shear flow over a two-dimensional mountain. Part I: General linear criteria. *J. Atmos. Sci.* **1999**, *56*, 412–436. [CrossRef]
16. Dörnbrack, A. Turbulent mixing by breaking gravity waves. *J. Fluid Mech.* **1998**, *375*, 113–141. [CrossRef]
17. Doyle, J.D.; Durran, D.R. Rotor and subrotor dynamics in the lee of three-dimensional terrain. *J. Atmos. Sci.* **2007**, *64*, 4202–4221. [CrossRef]
18. Vosper, S.B. Inversion effects on mountain lee waves. *Q. J. R. Meteorol. Soc.* **2004**, *130*, 1723–1748. [CrossRef]
19. Hertenstein, R.F.; Kuettner, J.P. Rotor types associated with steep lee topography: Influence of the wind profile. *Tellus* **2005**, *57*, 117–135. [CrossRef]
20. Hertenstein, R.F. The influence of inversions on rotors. *Mon. Weather Rev.* **2009**, *137*, 433–446. [CrossRef]
21. French, J.R.; Haimov, S.J.; Oolman, L.D.; Grubišić, V.; Serafin, S.; Strauss, L. Wave-induced boundary-layer separation in the lee of the Medicine Bow Mountains. Part I: Observations. *J. Atmos. Sci.* **2015**, *72*, 4845–4863. [CrossRef]
22. Grubišić, V.; Serafin, S.; Strauss, L.; Haimov, S.J.; French, J.R.; Oolman, L.D. Wave-induced boundary layer separation in the lee of the medicine bow mountains. Part II: Numerical modeling. *J. Atmos. Sci.* **2015**, *72*, 4865–4884. [CrossRef]
23. Strauss, L.; Serafin, S.; Haimov, S.; Grubišić, V. Turbulence in breaking mountain waves and atmospheric rotors estimated from airborne in situ and Doppler radar measurements. *Q. J. R. Meteorol. Soc.* **2015**, *141*, 3207–3225. [CrossRef] [PubMed]
24. Pokharel, B.; Geerts, B. A multi-sensor study of the impact of ground-based glaciogenic seeding on clouds and precipitation over mountains in Wyoming. Part I: Project description. *Atmos. Res.* **2016**, *182*, 269–281. [CrossRef]
25. Geerts, B.; Pokharel, B.; Kristovich, D. Blowing snow as a natural glaciogenic cloud seeding mechanism. *Mon. Weather Rev.* **2015a**, *143*, 5017–5033. [CrossRef]
26. Locatelli, J.D.; Hobbs, P.V. Fall speeds and masses of solid precipitation particles. *J. Geophys. Res.* **1974**, *79*, 2185–2197. [CrossRef]
27. Mitchell, D.L. Use of mass- and area-dimensional power laws for determining precipitation particle terminal velocities. *J. Atmos. Sci.* **1996**, *53*, 1710–1723. [CrossRef]
28. Damiani, R.; Haimov, S. A high-resolution dual-Doppler technique for fixed multiantenna airborne radar. *IEEE Trans. Geosci. Remote Sens.* **2006**, *44*, 3475–3489. [CrossRef]
29. Geerts, B.; Damiani, R.; Haimov, S. Finescale vertical structure of a cold front as revealed by an airborne Doppler radar. *Mon. Weather Rev.* **2006**, *134*, 251–271. [CrossRef]
30. Geerts, B.; Miao, Q.; Yang, Y. Boundary layer turbulence and orographic precipitation growth in cold clouds: Evidence from profiling airborne radar data. *J. Atmos. Sci.* **2011**, *68*, 2344–2365. [CrossRef]
31. Geerts, B.; Yang, Y.; Rasmussen, R.; Haimov, S.; Pokharel, B. Snow growth and transport patterns in orographic storms as estimated from airborne vertical-plane dual-doppler radar data. *Mon. Weather Rev.* **2015**, *143*, 644–665. [CrossRef]
32. Yang, Q.; Geerts, B. Horizontal convective rolls in cold air over water: Buoyancy characteristics of coherent plumes detected by an airborne radar. *Mon. Weather Rev.* **2006**, *134*, 2373–2396. [CrossRef]

33. Miao, Q.; Geerts, B. Finescale vertical structure and dynamics of some dryline boundaries observed in IHOP. *Mon. Weather Rev.* **2007**, *135*, 4161–4184. [CrossRef]
34. Sipprell, B.D.; Geerts, B. Finescale vertical structure and evolution of a preconvective dryline on 19 June 2002. *Mon. Weather Rev.* **2007**, *135*, 2111–2134. [CrossRef]
35. Damiani, R.; Geerts, B.; Demko, J.; Haimov, S.; French, J.; Zehnder, J.; Razdan, A.; Hu, J.; Petti, J.; Leuthold, M.; et al. The Cumulus, Photogrammetric, In Situ, and Doppler Observations Experiment of 2006. *Bull. Am. Meteorol. Soc.* **2008**, *89*, 57–73. [CrossRef]
36. Bergmaier, P.; Geerts, B. Airborne radar observations of lake-effect snowbands over the New York Finger Lakes. *Mon. Weather Rev.* **2016**, *144*, 3895–3914. [CrossRef]
37. Skamarock, W.C.; Klemp, J.B.; Dudhia, J.; Gill, D.O.; Barker, D.M.; Duda, M.G.; Huang, X.-Y.; Wang, W.; Powers, J.G. *A description of the Advanced Research WRF Version 3*; NCAR Technical Note, NCAR/TN-475+STR; Mesoscale and Microscale Meteorology Division, National Center for Atmospheric Research: Boulder, CO, USA, 2008.
38. Janjic, Z.I. Nonsingular Implementation of the Mellor–Yamada Level 2.5 Scheme in the NCEP Meso model. *NCEP Off. Note* **2002**, *437*, 61.
39. Lim, J.-O.J.; Hong, S.-Y. Development of an effective double-moment cloud microphysics scheme with prognostic Cloud Condensation Nuclei (CCN) for weather and climate models. *Mon. Weather Rev.* **2010**, *138*, 1587–1612. [CrossRef]
40. Mlawer, E.J.; Taubman, S.J.; Brown, P.D.; Iacono, M.J.; Clough, S.A. Radiative transfer for inhomogeneous atmospheres: RRTM, a validated correlated-k model of the longwave. *J. Geophys. Res.* **1997**, *102*, 16636–16682. [CrossRef]
41. Dudhia, J. Numerical study of convection observed during the Winter Monsoon Experiment using a mesoscale tow-dimensional model. *J. Atmos. Sci.* **1989**, *46*, 3077–3107. [CrossRef]
42. Sharman, R.D.; Trier, S.B.; Lane, T.P.; Doyle, J.D. Sources and dynamics of turbulence in the upper troposphere and lower stratosphere: A review. *Geophys. Res. Lett.* **2012**, *39*, L12803. [CrossRef]
43. Jing, X.; Geerts, B.; Friedrich, K.; Pokharel, B. Dual-polarization radar data analysis of the impact of ground-based glaciogenic seeding on winter orographic clouds. *Part I: Mostly Stratif. Clouds J. Appl. Meteorol. Climatol.* **2015**, *54*, 1944–1969.
44. Kirshbaum, D.J.; Durran, D.R. Factors governing cellular convection in orographic precipitation. *J. Atmos. Sci.* **2004**, *61*, 682–698. [CrossRef]
45. Baines, P.G. *Topographic Effects in Stratified Flows*; Cambridge University Press: Cambridge University, UK, 1995.
46. Regmi, R.; Kitada, T.; Dudhia, J.; Maharjan, S. Large-scale gravity current over the middle hills of Nepal Himalaya: Implications for aircraft accident. *J. Appl. Meteorol. Climatol.* **2017**. [CrossRef]
47. MacCready, P.B.J. Standardization of gustiness values from aircraft. *J. Appl. Meteor.* **1964**, *3*, 439–449. [CrossRef]
48. Sharman, R.D.; Cornman, L.B.; Meymaris, G.; Pearson, J.; Farrar, T. Description and derived climatologies of automated in situ eddy-dissipation-rate reports of atmospheric turbulence. *J. Appl. Meteorol. Climatol.* **2014**, *53*, 1416–1432. [CrossRef]
49. Reinecke, P.A.; Durran, D.R. Initial-condition sensitivities and the predictability of downslope winds. *J. Atmos. Sci.* **2009**, *66*, 3401–3418. [CrossRef]
50. Doyle, J.D.; Gaberšek, S.; Jiang, Q.; Bernardet, L.; Brown, J.M.; Dörnbrack, A.; Filaus, E.; Grubišić, V.; Kirshbaum, D.J.; Knoth, O.; et al. An intercomparison of T-REX mountain-wave simulations and implications for mesoscale predictability. *Mon. Weather Rev.* **2011**, *139*, 2811–2831. [CrossRef]
51. Smith, R.B. Aerial observations of the Yugoslavian bora. *J. Atmos. Sci.* **1987**, *44*, 269–297. [CrossRef]
52. Darby, L.S.; Poulos, G.S. The evolution of lee-wave-rotor activity in the lee of Pike's Peak under the influence of a cold frontal passage: Implications for aircraft safety. *Mon. Weather Rev.* **2006**, *134*, 2857–2876. [CrossRef]
53. Brinkmann, W.A.R. Strong downslope winds at Boulder, Colorado. *Mon. Weather Rev.* **1974**, *102*, 592–602. [CrossRef]